



**HAL**  
open science

# Full-field strain investigation of twinned martensite in a thermally activated Cu–Al–Ni single crystal using Localized Spectrum Analysis

Adrien Vinel, Maël Laquet, Xavier Balandraud, Benoît Blaysat, Michel Grédiac, Thomas Jailin

## ► To cite this version:

Adrien Vinel, Maël Laquet, Xavier Balandraud, Benoît Blaysat, Michel Grédiac, et al.. Full-field strain investigation of twinned martensite in a thermally activated Cu–Al–Ni single crystal using Localized Spectrum Analysis. *Acta Materialia*, 2024, 264, pp.119550. 10.1016/j.actamat.2023.119550. hal-04335374

**HAL Id: hal-04335374**

**<https://hal.science/hal-04335374v1>**

Submitted on 11 Dec 2023

**HAL** is a multi-disciplinary open access archive for the deposit and dissemination of scientific research documents, whether they are published or not. The documents may come from teaching and research institutions in France or abroad, or from public or private research centers.

L'archive ouverte pluridisciplinaire **HAL**, est destinée au dépôt et à la diffusion de documents scientifiques de niveau recherche, publiés ou non, émanant des établissements d'enseignement et de recherche français ou étrangers, des laboratoires publics ou privés.

# Full-field strain investigation of twinned martensite in a thermally activated Cu-Al-Ni single crystal using Localized Spectrum Analysis

Adrien Vinel<sup>a</sup>, Maël Laquet<sup>b</sup>, Xavier Balandraud<sup>a</sup>, Benoît Blaysat<sup>a</sup>, Michel Grédiac<sup>a</sup> and Thomas Jailin<sup>a</sup>

<sup>a</sup>Clermont Auvergne Université, Clermont Auvergne INP, CNRS, Institut Pascal, F-63000 Clermont-Ferrand, France

<sup>b</sup>Ecole Normale Supérieure de Rennes (ENS Rennes), F-35170 Bruz, France

## ARTICLE INFO

### Keywords:

Shape memory alloy  
Austenite-to-martensite phase transformation  
Strain distribution  
Cu–Al–Ni  
Deformation twinning  
Full-field measurement

## ABSTRACT


The paper presents a full-field strain analysis of the appearance/disappearance of twinned martensite in a Cu-Al-Ni single crystal subjected to thermal cycles. Localized Spectrum Analysis (LSA) was employed to process images of a checkerboard pattern preprinted on the sample's surface, enabling us to obtain strain maps with a suitable trade-off between strain resolution ( $2 \times 10^{-4}$ ) and spatial resolution (0.26 mm). During the cooling of the initially austenitic sample, habit plane variants (HPVs) were identified from the in-plane components of their mean right strain tensor. The match between measured data and theoretical expectations enabled us to measure the stretch parameters associated with the cubic-to-orthorhombic transformation occurring in the material. Various deformation mechanisms were revealed by an analysis in the strain space. In particular, the process of martensite appearance during cooling appeared to be based on the coordinated activation of HPV pairs whose strain levels globally compensate each other. Elastic strain gradients were also evidenced, highlighting the need for additional deformation to achieve kinematic compatibility at microstructure interfaces. Lastly, several thermal cycles were applied to the previously-trained sample, enabling us to quantify the level of spatio-temporal repeatability of the phase transformation.

## 1. Introduction

The special thermomechanical properties of shape memory alloys (SMAs) result from a reversible solid-solid phase transformation that can be induced by thermal and mechanical loading [1]. The high-temperature parent phase (*austenite*) has a cubic symmetry in all known SMAs, whereas the low-temperature product phase (*martensite*) has a lower symmetry, *e.g.* tetragonal, orthorhombic or monoclinic depending on the chemical composition of the alloy. In addition, due to the symmetries of the cubic cell, different *variants of martensite* can be created from a crystal of austenite. They correspond to the same unit cell, but oriented differently in space with respect to the parent cubic cell. The number of martensite variants depends on the level of symmetry breaking between the two phases. It is, for instance, equal to 6 for an orthorhombic martensite [2; 3; 4], corresponding to the case considered in the present study. If the austenite crystal is taken as the reference state (undeformed state), each martensite variant is associated with one characteristic transformation strain tensor, rotationally related to those of the other variants. Within a SMA sample, the two phases coexist in a certain range of stresses and temperatures. The large “strain jump” between austenite and martensite, typically several percent, leads to specific martensitic microstructures. These correspond to spatial arrangements of the martensite variants ensuring the continuity of displacements at the interfaces in the sense of continuum mechanics, while minimizing the total energy of the SMA sample. From the 1950s to the 1980s, pioneering work allowed progress in the understanding of kinematic and

energetic aspects of martensitic microstructures: see Refs [5; 6; 7; 8; 9; 10]. The Hadamard equation has been employed to express the kinematic compatibility between two variants of martensite (referred to as *martensite twins*) and between austenite and a twinned region (the interface being referred to as *habit plane*). From the 1990s on, several studies focused on more complex microstructures, involving several twinned regions and several habit planes, such as wedge-, X- or diamond-shaped configurations. All the martensite symmetries have been considered to cover all SMA categories. The main results are gathered in Refs [2; 4]. A key result of these theoretical studies is that the kinematic compatibility of complex microstructures is not possible without involving internal stresses. A phase transformation is associated with characteristic stress-free atom movements, but additional deformations may be required to ensure kinetic compatibility at the microstructure interfaces. In particular, compatibility stresses arise at the interfaces. Since the 2000s, several works have extended the theoretical analysis of low-energy morphologies. Various aspects have been considered in the literature (see for instance Refs [11; 12; 13; 14; 15; 16; 17; 18; 19; 20; 21; 22; 23; 24; 25; 26]): local elastic energy due to incompatibility between the austenite and each individual martensite variant (microstrains along each habit plane), twin boundary energy, twinning disconnection energy, dissipation energy, as well as elastic energy due to the global compatibility of the multi-domains within the SMA sample. The level of reversibility of the phase transformation is linked to potential anelastic effects. In this context, the experimental measurement of strain fields in martensitic microstructures is of prime interest. The aim of the present study is to analyze the distribution of the strains

\*Xavier Balandraud

 xavier.balandraud@sigma-clermont.fr (X. Balandraud)

in a SMA single crystal using a full-field measurement technique, namely Localized Spectrum Analysis (LSA), whose spatial resolution enables *mean* strains to be captured within twinned regions.

In recent decades, full-field measurement techniques have profoundly impacted the community of the mechanics and materials science of SMAs [27]. Indeed, strain and temperature phenomena are generally localized and spatially distributed within a SMA sample, making the use of visible and infrared cameras respectively for analyzing the spatio-temporal kinetics of the phase transformation useful. Digital image correlation (DIC) is a versatile technique for strain field measurement, and is now widely used in the experimental mechanics community. With this technique, a random pattern deposited onto the surface of the material sample is generally required. DIC is user-friendly and has enabled the community to go further in the understanding of deformations in SMAs. Applications have mainly concerned polycrystals. However, the review dating from 2021 in Ref. [27] identified 50 references dealing with DIC measurement on single crystals, among which only 8 concerning Cu-Al-Ni, which is the alloy considered in the present study. Single-crystal samples are more difficult to obtain from suppliers than polycrystal ones. However, they give access to the “elementary” microstructures which are at the basis of the SMA properties. Although a powerful tool, DIC has some disadvantages. This is particularly true when a good compromise must be reached between spatial and measurement resolutions, which is crucial for an analysis of sharp details in strain maps. First, random speckles do not constitute the optimal pattern with respect to sensor noise propagation [28]. Furthermore, the use of a random pattern gives rise to a pattern-induced bias [29], especially in case of high-frequency strain distribution [30], which is the case with the martensitic microstructures in SMAs. The present study proposes to use another full-field measurement technique to extract strain maps at the material surface: LSA. This method relies on a periodic pattern previously deposited on the material sample surface. Image processing is then based on the Windowed Fourier Transform (WFT) of the undeformed (reference) and deformed images of the pattern. It is worth pointing out that LSA has rarely been used with SMAs; only three times to our knowledge: see Refs [31; 32; 33].

The objective of the present study is to perform a full-field strain analysis of the appearance/disappearance of twinned regions in a Cu-Al-Ni single crystal subjected to thermal cycles using LSA. Note that a checkerboard pattern was placed on the sample surface because this pattern leads to the best metrological performance [34]. Using a period of 60  $\mu\text{m}$  for the checkerboard, the spatial resolution of the technique enabled us to measure the projection onto the observed plane of the *mean* right strain tensors  $\underline{U}$  associated with the different finely-twinned martensite regions, facilitating various analyses of the spatio-temporal

kinetics of transformation. It was for instance possible to identify the stretch parameters associated with the cubic-to-orthorhombic transformation occurring during the cooling of the alloy (Section 4.2). Various deformation mechanisms were revealed by the analysis in the strain space. In particular, the process of martensite appearance during cooling appeared to be based on the coordinated activation of pairs of twinned regions whose strain levels globally compensate each other (Section 4.3). The self-accommodating nature of the transformation was also examined on the basis of the proportions of the twinned regions activated during the temperature-induced transformation (Sections 4.4 and 4.6). Elastic strain gradients were also evidenced, highlighting the need for additional deformation to achieve kinematic compatibility at the microstructure interfaces (Section 4.5). Lastly, several thermal cycles were applied to the previously-trained sample, enabling us to quantify the level of spatio-temporal repeatability of the phase transformation kinetics (Section 4.7).

The following notations are used throughout the paper to represent quantities. Second-order tensors (matrices) are indicated by a double underline, *e.g.*  $\underline{\underline{U}}$ . First-order tensors (vectors) are indicated by a single underline, *e.g.*  $\underline{u}$ . A hat above a vector indicates that it is unitary, *e.g.*  $\hat{n}$ . Zero-order tensors (scalars) are not underlined, *e.g.*  $\alpha$ . Operator  $\otimes$  corresponds to the tensor product of vectors such that  $(\underline{a} \otimes \underline{b})_{ij} = a_i b_j$ .

## 2. Material and methods

### 2.1. Sample

The sample under study was a Cu-Al<sub>13.9</sub>-Ni<sub>4.6</sub> (wt.%) single crystal developed by Nimesis Technology, Metz, France. First, a 33 mm diameter cylindrical ingot was elaborated using the Bridgman method. This produced an austenite crystal, one of whose cubic axes, say [001], corresponds to the axis of the ingot. The latter was then cut perpendicularly to its axis and polished to obtain a 3 mm thick slice: see Fig. 1-a showing the sample partially transformed into martensite by cooling with a Peltier cell.

The composition in atomic percentages gives Cu<sub>68.36</sub>-Al<sub>27.46</sub>-Ni<sub>4.18</sub>, which enables us to estimate the number of electrons per atom: 1.55. For Cu-Al-Ni alloys, the eutectic point that separates samples transforming to  $\beta'$  martensite (monoclinic,  $\approx 18\text{R}$ ) and samples transforming to  $\gamma'$  martensite (orthorhombic,  $\approx 2\text{H}$ ) corresponds to a ratio of 1.53 [35; 36]. Consequently, the austenite of the alloy under study was expected to transform into orthorhombic martensite when cooling. The DSC curve provided by the supplier (not shown here) gave the following transformation temperatures with the tangent method:  $M_f = -20^\circ\text{C}$ ,  $M_s = -12^\circ\text{C}$ ,  $A_s = 35^\circ\text{C}$  and  $A_f = 41^\circ\text{C}$ . Note that the empirical formula from the chemical composition in Ref. [37] gives  $M_s = -3.5^\circ\text{C}$ . Our observations of the microstructure (visually and by camera) showed discrepancies with the DSC results. The latter gives by construction lower values of  $M_s$ . Here,

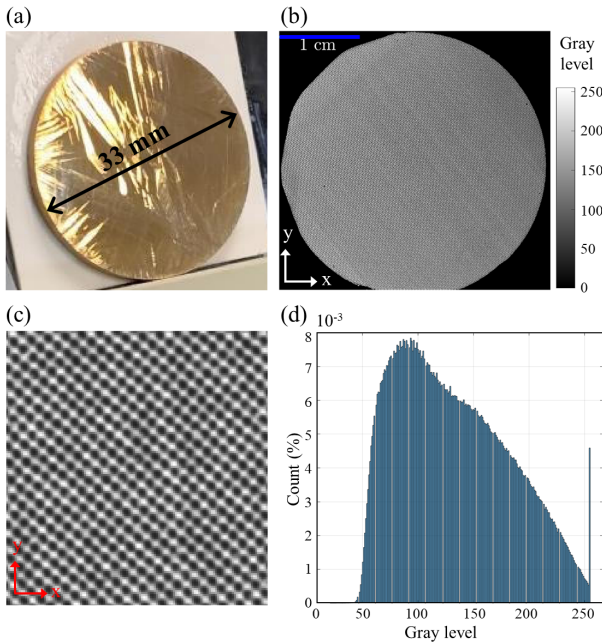


**Figure 1:** (a) Sample partially transformed into martensite; (b) austenitic sample covered with a checkerboard pattern created with a laser marker after pre-painting in white; (c) close-up of the periodic pattern having a period of  $60\ \mu\text{m}$ ; (d) distribution of gray levels over the surface of the sample.

the first needles and wedges of martensite actually appeared at about  $10^\circ\text{C}$  during cooling. More surprisingly, more than half of the sample appeared to be transformed into martensite at about  $0^\circ\text{C}$  during cooling, while the  $M_s$  value measured by DSC is considerably lower ( $-12^\circ\text{C}$ ). These discrepancies with the DSC results may be due to differences in the temperature rates used, material aging, or training with transformation cycles, as well as large sample-to-sample variations due to the presence of impurities, residual stresses or precipitated phases. In any case, the sample can be either austenitic, martensitic, or a mix of the two phases at room temperature (here  $\approx 23^\circ\text{C}$ ) depending on its thermal history. In the present study, the sample was initialized to the austenitic state at room temperature, which is considered as the reference state (no strain) for the analyses.

The lattice parameters of both austenite and martensite cells are rarely given in the literature for a given chemical composition. Moreover, the values are generally measured at different temperatures, namely a high temperature for the austenite and a low temperature for the martensite. Values are provided in Ref. [38] for an alloy with a composition of  $\text{Cu-Al}_{14.2}\text{-Ni}_{4.3}$  (wt.%), *i.e.* close to our alloy:  $a_0 = 5.836\ \text{\AA}$  for the cubic cell of the austenite; and  $a = 4.382\ \text{\AA}$ ,  $b = 5.356\ \text{\AA}$  and  $c = 4.222\ \text{\AA}$  for the martensitic orthorhombic cell. Note that the lattice correspondence of the cubic to orthorhombic transformation occurring in Cu-Al-Ni alloys is  $[110]_{\text{aust}} \parallel [100]_{\text{mart}}$ . The lattice parameter values enable us to calculate the so-called *stretch parameters*, denoted by  $\alpha$ ,  $\beta$ ,  $\gamma$  in the rest of the paper, of the cubic-to-orthorhombic

transformation [2]:  $\alpha = \sqrt{2}b/a_0 = 1.0619$ ,  $\beta = b/a_0 = 0.9178$  and  $\gamma = \sqrt{2}b/a_0 = 1.0231$  [38; 39]. Refined values identified with our strain measurements using LSA will be given in Section 4.2 for the alloy under study.

## 2.2. Surface preparation

The full-field measurement technique used in this work requires a periodic pattern, such as grid or a checkerboard, on the surface of the plane sample of material. Several techniques allow periodic patterns to be deposited with periods ranging from a few millimeters [40; 41; 42] to a few micrometers [43; 44]. Piro and Grédiac developed a method to deposit grids with periods of about  $50\ \mu\text{m}$  from preprinted sheet and adhesive [45]. More recently, Bouyra *et al.* investigated the use of a laser marking machine to engrave a checkerboard on a material sample [46]. Through an in-depth study of the influence of the machine's parameters, they were able to engrave checkerboards comprised of squares of  $50\ \mu\text{m}$  width. The main advantage of using a laser marking machine is its ease of use once the printer settings are optimized. Note that the method requires a thin coat of paint to be deposited beforehand. For the present study, a MDU1000C laser marker from Keyence was used to prepare the surface of the SMA sample. It is equipped with a  $\text{YVO}_4$  UV laser with a wavelength of  $355\ \text{nm}$ . The laser dot size was estimated at approximately  $30\ \mu\text{m}$ . Hence the scan speed and pulse frequency were chosen to obtain squares every  $60\ \mu\text{m}$ , which is the smallest value that can be obtained using this device with these settings. Similarly to what was done in Ref. [46], several combinations of printing parameters were tested. The set of parameters leading to the best results were: laser power = 50%; scan speed (speed of the laser spot) =  $3600\ \text{mm s}^{-1}$ ; pulse frequency = 60 kHz; repetition (number of times that the same pattern is engraved at the same place) = 40; and spot variation (defocus of the laser spot) = 0 mm. Using these parameters, the sample surface was engraved in less than 10 min. Note that this operation was performed on the sample in austenite state. Initialization to the austenite state was obtained by heating the sample above  $60^\circ\text{C}$ , followed by natural cooling to room temperature. A few martensite needles sometimes reappeared during this cooling phase, but their small size did not penalize the study. Figure 1-b shows the checkerboard engraved on the SMA sample previously painted in white. Figure 1-c shows a close-up view of the pattern. Note that a small angle was deliberately applied with respect to the  $x$ -axis (horizontal axis of the grid of the camera) to avoid aliasing effects in the images [47]. Figure 1-d shows the distribution of gray levels over the surface obtained by setting the integration time so that the largest dynamic sensor range is obtained; see next section.

## 2.3. Imaging system

Microstructure variations in the sample during thermal cycles were tracked using a Prosilica GT 6600 camera with a CCD sensor of  $6576 \times 4384$  pixels<sup>2</sup> (28 Mpixels), recording images encoded with a gray depth equal to 8 bits. The field

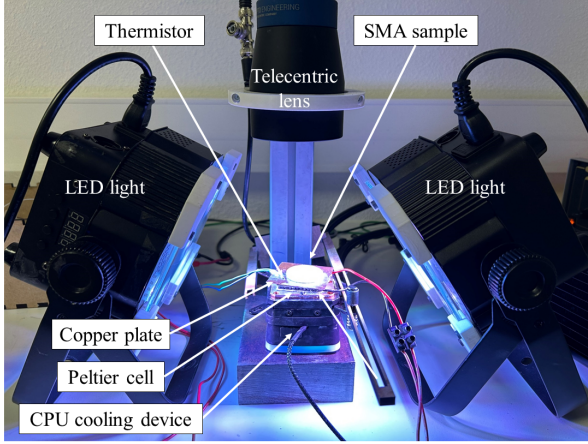


**Figure 2:** Photo of the experimental setup.

**Table 1**  
Imaging hardware parameters.

Camera	Prosilica GT 6600
Image resolution	6576 × 4384 pixels <sup>2</sup>
Dynamic range, detector	8 bits
Acquisition rate	1 fps
Integration time	IT = 8 ms
Lens	TC16M048
Magnification	0.75
Aperture	f/16
Field of view	48.4 mm × 32.2 mm
Image scale	1 pixel = 7.36 μm
Stand-off distance	50 cm
Patterning technique	Laser-marked checkerboard
Pattern period size	5.78 pixels

of view was 48.4 mm × 32.2 mm, which thus allowed us to observe almost the entire surface of the sample. Only a very small area at the bottom of the image is not visible in Fig. 1-b. The image scale was 1 pixel = 7.36 μm. The square width of the checkerboard corresponded thus to 4.08 pixels. The integration time was 8 ms and the acquisition rate was fixed to 1 frame per second. A TC16M048 telecentric lens from Opto-engineering was used. Finally, note that the sample was illuminated using two LED light sources. Figure 2 shows the experimental setup. Table 1 summarizes the imaging hardware parameters.

## 2.4. Thermal loading

Thermal cycles were applied to the sample in order to study the appearance and disappearance of the martensitic microstructures upon cooling and heating, respectively. Temperature changes were imposed using a Peltier Cell (Adaptive 8.8V, 13.1A, 72W, 40 × 40 mm<sup>2</sup>) and a thin copper plate in contact with one face of the sample. To ensure that the other face of the Peltier cell remained at room temperature, contact was made with a cooling device designed for computer Central Processing Units (CPU), namely an Aquafusion 360 series. An electronic setup involving an Arduino card, a Mosfet driver and a

thermistor was developed to control the voltage and current given as inputs to the Peltier cell. Moreover, to avoid any synchronization issues, the Arduino card was used to send a trigger to the camera for each image acquisition and to record the temperature at the same time.

Starting from the austenitic state at room temperature, three cooling-heating cycles were applied as follows while images were captured by the camera:

- Cooling to about −1 °C in around 300 s in order to create martensite — Note that preliminary tests with lower temperatures (not presented here) led to condensation at the sample surface, preventing the correct measurement of the strain fields;
- Heating to about 45 °C, also in around 300 s, in order to return to the austenitic state — Note that slight overheating occurred before stabilizing at 45 °C (see the videos in supplementary material).

It should be noted that the sample had previously been subjected to numerous thermal cycles (over 100) prior to the camera measurements. A stabilized response was *a priori* expected during the three cycles observed by the camera.

## 2.5. Extracting the right strain tensor distributions

In Ref. [28], it has been shown that checkerboards are optimal patterns for kinematic full-field measurement. Indeed, the noise in the strain fields is inversely proportional to the sum of squares of SubSet Intensity Gradient (SSIG) [48], which is maximized with a checkerboard pattern. In Ref. [49], the authors adapted the LSA method (initially used to process 2D grids [50]) in order to extract strain fields from checkerboards. Furthermore, Ref. [51] presents a comparison of three techniques, namely Geometric Phase Analysis (GPA), the Windowed version of Geometric Phase Analysis (WGPA) and LSA. Using synthetic image deformation, the metrological performance was compared with respect to a metric defined in the paper. It was found that LSA provides a good compromise between metrological performance and computation time.

In the present study, the LSA technique was used to extract the strain fields from reference and deformed checkerboard images. The principle, thoroughly described in Ref. [49], is briefly recalled here. A checkerboard can be considered as a grid of diamonds along the directions of the diagonals of the squares forming it. Let  $f$  be the spatial frequency of the periodic pattern. The method consists in computing the WFT of the image only for this frequency. Thus:

$$\hat{s}_g(x, y, \theta) = \int_{-\infty}^{+\infty} \int_{-\infty}^{+\infty} s(\eta, \xi) g(x - \eta, y - \xi) e^{-2i\pi f(x\cos(\theta) + y\sin(\theta))} d\eta d\xi, \quad (1)$$

where  $s$  is the gray level distribution of the image and  $\theta$  an angle with respect to the horizontal axis  $x$  (it defines the

direction along which the displacements will be measured).  $g$  is a Gaussian window centered at the pixel of coordinates  $(x, y)$  where the quantity  $\hat{s}_g(x, y, \theta)$  is computed:

$$g(x, y) = \frac{1}{2\pi\sigma^2} e^{-\frac{x^2+y^2}{2\sigma^2}}, \quad (2)$$

where  $\sigma$  is the standard deviation of the Gaussian.

The WFT is estimated for the two values of  $\theta$  defined by the two diagonals of the squares forming the checkerboard. Two distributions of complex numbers are obtained after these two WFTs. Their arguments correspond to the phases along these two directions. These phases are then expressed in the  $x$ - $y$  coordinate system. The sought displacements are proportional to the phase change between the reference state (here, the austenitic state at room temperature) and the current state. Thus:

$$\underline{\tilde{u}}(\underline{x}) = -\frac{1}{2\pi f} \left( \underline{\tilde{\Phi}}^{\text{curr}}(\underline{x} + \underline{\tilde{u}}(\underline{x})) - \underline{\tilde{\Phi}}^{\text{ref}}(\underline{x}) \right), \quad (3)$$

where  $\underline{\tilde{u}}$  is the sought displacement,  $\underline{x}$  the position vector whose components are  $(x, y)$ , and  $\underline{\tilde{\Phi}}^{\text{curr}}$  and  $\underline{\tilde{\Phi}}^{\text{ref}}$  the current and reference phases, respectively. The tildes above the quantities denote the fact that the phases and displacements obtained are not exactly the true ones, but are the true ones convolved with the Gaussian window  $g$  [52]. Since the displacement vector  $\underline{\tilde{u}}$  is involved in both sides of Eq. 3, a fixed-point algorithm is used to solve this equation. Then the fields of the in-plane component of the deformation gradient  $\underline{F}$  can be derived pixelwise from the displacements assessed. Finally, the corresponding fields for the right strain tensor  $\underline{U}$  are calculated from  $\underline{U} = \sqrt{\underline{F}\underline{F}^T}$ .

50 images of the sample were taken in the austenite state at room temperature to assess metrological performance in experimental conditions. With a flawless device, the right strain tensor  $\underline{U}$  should in theory remain equal to the identity matrix. The displacement fields were then extracted with  $\sigma$  set to 6 pixels, which gives an apparent size for the Gaussian equal to  $6\sigma$ , *i.e.* 0.265 mm [53]. This value corresponds to the spatial resolution of the maps shown in this paper. It means that in case of sharp interfaces between austenite and twinned zones, or between twinned zones themselves, LSA smooths the fields near these interfaces. Next, the fields of the three in-plane components  $U_{xx} (\approx 1)$ ,  $U_{yy} (\approx 1)$  and  $U_{xy} (\approx 0)$  were computed. The standard deviation (std) of the noise affecting each quantity was then computed pixelwise. Figure 3 shows histograms of the std for the three components. Finally, the equivalent standard deviation  $\sigma_{\text{eq}}$  of each quantity was calculated as follows [50]:

$$\sigma_{\text{eq}}(U_{uv}) = \sqrt{\frac{1}{N_{\text{pix}}} \sum_{k=1}^{N_{\text{pix}}} \text{std}^2(U_{uv}(x_k, y_k))}, \quad (4)$$

where  $U_{uv}$  is any of the three in-plane components of the right strain tensor,  $N_{\text{pix}}$  the number of pixels over the sample

surface, and  $(x_k, y_k)$  the pixel coordinate where the std is calculated. The equivalent standard deviations are the quantities of interest because they reflect the average noise level for each component of  $\underline{U}$ . The three values obtained for  $\sigma_{\text{eq}}$  are indicated in the graphs:  $2.05 \times 10^{-4}$  and  $1.97 \times 10^{-4}$  for the  $U_{xx}$  and  $U_{yy}$  components, respectively, and  $1.41 \times 10^{-4}$  for the  $U_{xy}$  component. They are of the same order of magnitude as that classically obtained with this technique; see Refs [49; 34; 46]. It can be verified that the measurement resolution for the  $xy$  component is approximately  $1/\sqrt{2}$  times that of the  $xx$  or  $yy$  component.

### 3. Strains associated with the cubic-to-orthorhombic transformation

We recall here some basics concerning the kinematics of cubic-to-orthorhombic (C-O) microstructures with  $[110]_{\text{aust}} \parallel [100]_{\text{mart}}$  correspondence. This will enable us to analyze in the following sections the distribution of the three in-plane components of the right strain tensor  $\underline{U}$  measured over the sample surface. More details about martensitic microstructures can be found in Refs [2; 4; 10].

*Variants of martensite* — Due to the symmetry breaking induced by the C-O transition, six variants of martensite can form from an austenite crystal. Considering that the undeformed austenite is the reference state, these variants can be represented by the following six (stress-free) strain tensors  $\underline{U}_i$ , written here in the basis of the cubic axes of the austenite crystal ( $[100]$ ,  $[010]$ ,  $[001]$ ):

$$\begin{aligned} \underline{U}_1 &= \begin{pmatrix} \frac{\alpha+\gamma}{2} & 0 & \frac{\alpha-\gamma}{2} \\ 0 & \beta & 0 \\ \frac{\alpha-\gamma}{2} & 0 & \frac{\alpha+\gamma}{2} \end{pmatrix}, \quad \underline{U}_2 = \begin{pmatrix} \frac{\alpha+\gamma}{2} & 0 & \frac{-\alpha+\gamma}{2} \\ 0 & \beta & 0 \\ \frac{-\alpha+\gamma}{2} & 0 & \frac{\alpha+\gamma}{2} \end{pmatrix} \\ \underline{U}_3 &= \begin{pmatrix} \frac{\alpha+\gamma}{2} & \frac{\alpha-\gamma}{2} & 0 \\ \frac{\alpha-\gamma}{2} & \frac{\alpha+\gamma}{2} & 0 \\ 0 & 0 & \beta \end{pmatrix}, \quad \underline{U}_4 = \begin{pmatrix} \frac{\alpha+\gamma}{2} & \frac{-\alpha+\gamma}{2} & 0 \\ \frac{-\alpha+\gamma}{2} & \frac{\alpha+\gamma}{2} & 0 \\ 0 & 0 & \beta \end{pmatrix} \\ \underline{U}_5 &= \begin{pmatrix} \beta & 0 & 0 \\ 0 & \frac{\alpha+\gamma}{2} & \frac{\alpha-\gamma}{2} \\ 0 & \frac{\alpha-\gamma}{2} & \frac{\alpha+\gamma}{2} \end{pmatrix}, \quad \underline{U}_6 = \begin{pmatrix} \beta & 0 & 0 \\ 0 & \frac{\alpha+\gamma}{2} & \frac{-\alpha+\gamma}{2} \\ 0 & \frac{-\alpha+\gamma}{2} & \frac{\alpha+\gamma}{2} \end{pmatrix}. \end{aligned} \quad (5)$$

where  $\alpha$ ,  $\beta$  and  $\gamma$  are the stretch parameters defined above from the lattice parameters of austenite and martensite.

*Martensite twin* — A crystal of austenite can transform into two martensite variants  $i$  and  $j$  separated by a plane interface while maintaining the continuity of the displacement field. They form *martensite twins*. The corresponding compatibility equation between the two variants reads as follows:

$$\underline{Q}_{ij} \underline{U}_j - \underline{U}_i = \underline{a}_{ij} \otimes \hat{n}_{ij}, \quad (6)$$

where the unknowns are the rotation matrix  $\underline{Q}_{ij}$ , the so-called shear vector  $\underline{a}_{ij}$ , and the vector  $\hat{n}_{ij}$  which is the unit vector normal to the interface plane between the two zones in the reference configuration. Note that in the case of the

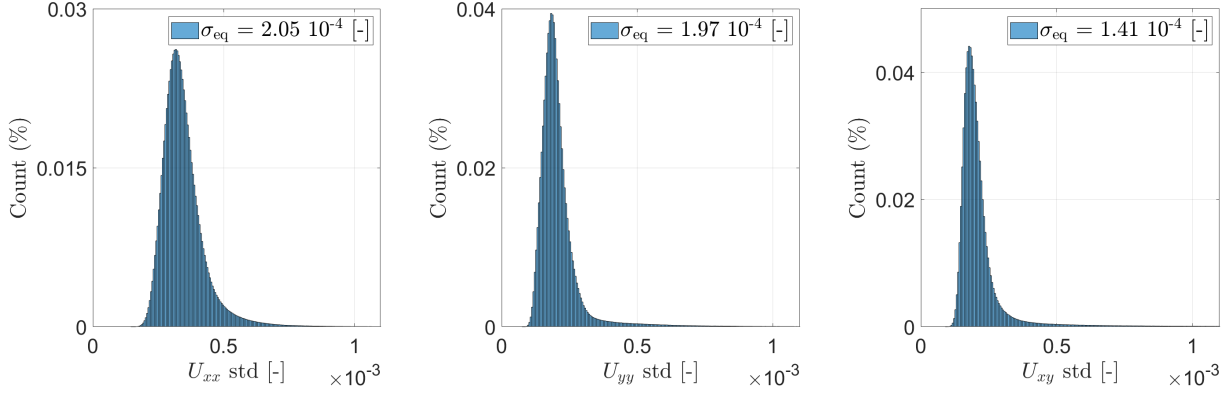


**Figure 3:** Assessment of the noise in the measurement of the three in-plane components of the right strain tensor  $\underline{U}$ : normalized histograms of the standard deviations (std) and equivalent standard deviations  $\sigma_{\text{eq}}$  measured from 50 images of the sample in the austenite state at room temperature.

C-O transformation, this equation always has two solutions, whatever the martensite twin ( $i, j$ ) considered. These solutions can be calculated from the analytical expressions given for instance in Ref. [2].

*Habit planes* — Compatibility between the austenite crystal and one single variant of martensite is not possible for the C-O transformation. A mix of two finely twinned variants is required to achieve “on average” compatibility with austenite through a habit plane. This mean compatibility is written:

$$\underline{F}_{ij} - \underline{I} = \underline{b}_{ij} \otimes \underline{\hat{m}}_{ij}, \quad (7)$$

$$\text{with } \underline{F}_{ij} = \underline{R}_{ij}[\lambda_{ij}\underline{Q}_{ij}\underline{U}_j - (1 - \lambda_{ij})\underline{U}_i], \quad (8)$$

where  $\underline{I}$  is the identity matrix (corresponding to the austenite) and  $\underline{F}_{ij}$  the average deformation gradient of the finely-twinned martensite with volume fractions  $\lambda_{ij}$  and  $1 - \lambda_{ij}$  for variants  $i$  and  $j$  respectively. Once Eq. 6 is solved, the unknowns are the rotation matrix  $\underline{R}_{ij}$ , the vector  $\underline{b}_{ij}$  and the habit-plane unit normal  $\underline{\hat{m}}_{ij}$ . Solutions exist in certain ranges of the stretch parameters; see formulas in Ref. [2]. For a given martensite twin ( $i, j$ ), up to 8 solutions can be obtained for Eqs 7-8. Considering all the pairs of martensite variants, up to 96 solutions can be obtained. The number depends on the stretch parameter values ( $\alpha, \beta, \gamma$ ).

Finally, once a solution to Eqs 7-8 is found, it is possible to calculate the *mean* right strain tensor  $\underline{U}_{ij}$  of the finely-twinned martensite zone by:

$$\underline{U}_{ij} = \sqrt{\underline{F}_{ij}\underline{F}_{ij}^T}. \quad (9)$$

With the lattice parameters of the alloy under study, and considering all the possibilities of pairs of martensite variants, 24 distinct matrices  $\underline{U}_{ij}$  are obtained. They are the right strain tensors of the martensitic zones that are expected to be measured at the scale of the optical measurement system used in the experiments, if the measurement resolution allows this.

## 4. Experimental results and discussion

Using the experimental apparatus described in Section 2, three temperature cycles were applied to the SMA sample to evaluate repeatability in the appearance and disappearance of the martensitic microstructures under cooling and heating, respectively. Sections 4.1 to 4.6 are focused on the first cycle. Various maps of right strain tensor components are presented and discussed. The stretch parameters of the alloy, and the orientation of the austenite crystal with respect to the global reference coordinate system of the camera, are also identified using the theory recalled in Section 3. Two questions are then discussed: how is the austenite deformed during the appearance of martensite? are the twinned regions equally distributed within the sample as expected for a temperature-induced transformation (“self-accommodating” martensite)? Finally, repeatability over the three thermal cycles is discussed in Section 4.7.

### 4.1. Preliminary observations

Video 1 in supplementary material shows variations in the three in-plane components of the right strain tensor  $\underline{U}$  throughout the first cooling-heating cycle. Maps of  $U_{xx}$ ,  $U_{xy}$  and  $U_{yy}$  are selected at three times in Fig. 4. The following comments can be made about these maps:

- When the sample reaches 5 °C during cooling, a few martensite wedges are visible (Figs 4a, 4d, 4g). They have developed from the circular boundary of the sample. In particular, a centimeter-sized martensite wedge is visible on the left-hand side. Interestingly, on one side of this wedge, the fields are heterogeneous: regular layering is visible at the scale of the observation (see arrow 1). Some groups of fine parallel martensite needles are also visible. Finally, while almost all the martensite appeared from the sample boundary, an isolated microstructure began to appear in the middle (see arrow 2);
- At the end of cooling (about −1 °C, Figs 4b, 4e and 4h), the majority of the sample is transformed to

martensite. Some of the wedges previously existing at 5 °C have grown, but most of the microstructures consist of groups of parallel needles. Diamond-like microstructures are also visible in the middle of the sample, especially in the  $U_{yy}$  map; see zone 3. The remaining austenite (in green on the maps) is found throughout the sample: it is finely distributed between the numerous martensite needles, as well as in some larger zones;

- At the end of heating (about 45 °C, Figs 4c, 4f and 4i), almost all the sample has returned to the austenitic state. A few residual microstructures consisting of isolated martensite needles remain. Two small martensite wedges are also visible in the upper right-hand part of the sample; see arrows 4. It can be noted that they were visible at 5 °C when the martensite started to appear in the sample during cooling (compare with the maps in Figs 4a, 4d, 4g). As can be seen in Video 1, the spatio-temporal kinetics of martensite appearance and disappearance are roughly symmetrical: the microstructures that appear first are generally those that disappear last;
- From profilometry measurements (not presented here), it was estimated that errors due to surface tilting of the martensitic zones are negligible compared to the transformation strain levels (order of magnitude of  $4 \times 10^{-2}$ ): maximum error lower than  $1 \times 10^{-3}$  for the centimeter-sized martensite wedge visible on the left-hand side of the specimen at the end of cooling.

A further analysis can be carried out by performing a study in strain space, as proposed below. Before doing this, the following section proposes a change of basis to display the strain components, while refining the values of the alloy's stretch parameters.

## 4.2. Identification of stretch parameters and change of basis

In Section 3, several equations governing martensitic microstructure kinematics were recalled. For a given set of stretch parameters ( $\alpha, \beta, \gamma$ ), it is thus possible to calculate the *mean* right strain tensors  $\underline{U}_{ij}$  of the twinned regions allowing compatibility with the austenite crystal. As indicated above, there is a sparse availability of stretch parameters available in the literature. Nevertheless, using the parameters given in Refs [38; 39] for the Cu-Al<sub>14.2</sub>-Ni<sub>4.3</sub> (wt.%) alloy, namely  $\alpha = 1.0619$ ,  $\beta = 0.9178$  and  $\gamma = 1.0231$ , the number of distinct  $\underline{U}_{ij}$  that are expected to appear within our SMA sample can be theoretically determined: 24. Figure 5 displays these theoretical *mean* right strain tensors in the  $\{U_{XX}, U_{YY}\}$  and  $\{U_{XX}, U_{XY}\}$  planes. Here,  $X$  and  $Y$  correspond to the [100] and [010] directions of the austenite cubic crystal, respectively. Out-of-plane components involving  $Z = [001] = z$  are not considered here as they cannot be compared with our experimental measures. The black dots represent the 24 calculated distinct tensors  $\underline{U}_{ij}$ . The figure is thus

a “visualization” in the  $\{U_{XX}, U_{YY}, U_{XY}\}$  space of the 24 twinned regions that are expected in a SMA with a similar composition to the present Cu-Al<sub>13.9</sub>-Ni<sub>4.6</sub> (wt.%) alloy. Note that half of the black dots are superimposed in the  $\{U_{XX}, U_{YY}\}$  plane (Fig. 5a). Moreover, it can be seen that some of the dots are relatively close to each other. Zooms on close dots are shown in the figure. The red circles around the dots have a diameter equal to 6 times the equivalent standard deviation  $\sigma_{eq}$  measured in Fig. 3 for each component (The so-called “3-sigma” rule was used here to define this diameter [53]). It is very likely that these close strain levels cannot be experimentally distinguished from each other. In practice, 12 distinct habit plane variants (HPVs) are identifiable with the measurement system used.

The in-plane components of the right strain tensors  $\underline{U}$  obtained experimentally during the test were initially expressed in the global reference system ( $x, y$ ) of the measurement grid of the camera. However, since the theoretical mean right strain tensors  $\underline{U}_{ij}$  are displayed in Fig. 5 using the basis of the austenite cubic cell, namely  $\underline{X} = [100]$  and  $\underline{Y} = [010]$ , it is logical to do the same for the experimental data. Since the  $Z = [001]$  direction of the austenite crystal is perpendicular to the surface of the specimen ( $Z = z$ ), there is an unknown rotation around this axis that should *a priori* match the experimental data with the theoretical data: it corresponds to the angle between the  $X$ - and  $x$ - axes. A minimization problem was solved to retrieve this angle as well as the stretch parameters of the alloy used in this study. It consisted in minimizing the distances between the centers of the experimental peaks and the theoretical points in the  $\{U_{XX}, U_{YY}, U_{XY}\}$  space. This problem was resolved by using the ‘fmincon’ Matlab function. This minimization led to the following values for the stretch parameters:  $\alpha = 1.0507$ ,  $\beta = 0.9272$  and  $\gamma = 1.0239$ . It can be noted that the product of these parameters, *i.e.* the determinant of any  $\underline{U}_i$  in Eq. 5, is equal to 0.9975. This value is close to 1, which is consistent with the fact that phase transformations in SMAs are isovolumic. Figure 6 shows the distribution of the measured right strain tensors  $\underline{U}$  at the end of the first cooling stage (about -1 °C), but recalculated in the basis of the austenite cubic cell from the knowledge of the angle between the two coordinate systems. The components are given in two planes, namely and  $\{U_{XX}, U_{YY}\}$  and  $\{U_{XX}, U_{XY}\}$ . The black dots represent the 12 theoretical mean right strain tensors of the twinned regions allowing compatibility with austenite, computed when using the identified stretch parameters and “grouping” close solutions. Austenite is also represented by a black dot at the center of the graphs. The theoretical martensite peaks, corresponding to the 12 identifiable HPVs, are numbered for identification purposes in the rest of the paper. Note that certain dots are superimposed in the  $\{U_{XX}, U_{YY}\}$  plane, for instance #1 and #2.

Other planes of representation can be used. For instance, displaying the distribution in the  $\{U_{XY}, U_{XX} - U_{XY}\}$  plane



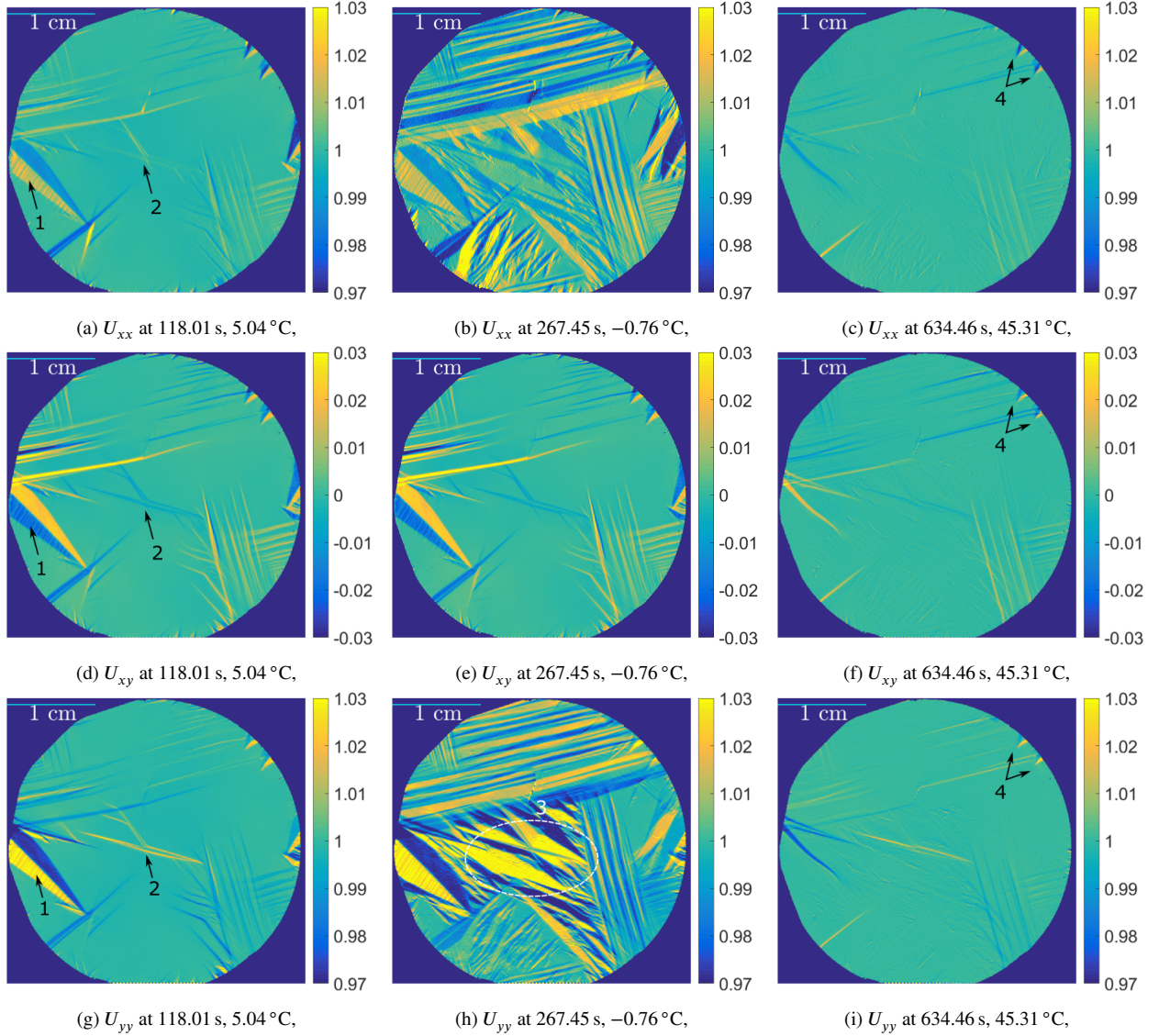


**Figure 4:** Maps of the in-plane components of the right strain tensor  $\underline{U}$  measured during the first thermal cycle. First column: at about 5 °C upon cooling. Second column: at the end of cooling (around -1 °C). Third column: at end of heating (around 45 °C).

(see Fig. 7) enables us to better isolate the theoretical HPVs. Indeed, this plane is orthogonal to the line  $U_{XX} + U_{YY} = \text{constant}$  (for example 1, which is an approximation to the isovolumetry condition).

Finally, before analyzing the experimental results in the next section, additional information can be provided about the  $(i, j)$  pairs of martensite variants that are potentially concerned in each of the 12 experimentally identifiable martensite peaks: see Table 2, where variant numbers in the second column correspond to those in Eq. 5. Three comments can be made about this table:

- The (1, 2), (3, 4) and (5, 6) twins are not involved. These correspond to so-called *compound* twins in the common classification used in crystallography [3];
- All the other pairs, each one offering two solutions classically referred to as *type-1* and *type-2* twins, are

concerned. As a reminder, the twin interface is a crystallographic (rational) plane in the former case; whereas for the latter case the interface is typically not rational. In the table, the type is labeled in superscript:  $(i, j)^I$  and  $(i, j)^{II}$  respectively;

- Each twin seems to appear twice for distinct martensite peaks, e.g., twin  $(1, 5)^I$  is involved both in #4 and #8. In fact, the two occurrences correspond to different variant proportions in Eq. 8. The proportion of variants 1 and 5 is 0.2907/0.7093 respectively for #4, while it is 0.7093/0.2907 for #8. Note that whatever the type of twin, the proportions are always nearly 0.3/0.7 and 0.7/0.3 with the stretch parameters of the considered alloy.

As a general remark from Table 2, since any martensite peak is potentially the consequence of the presence of the

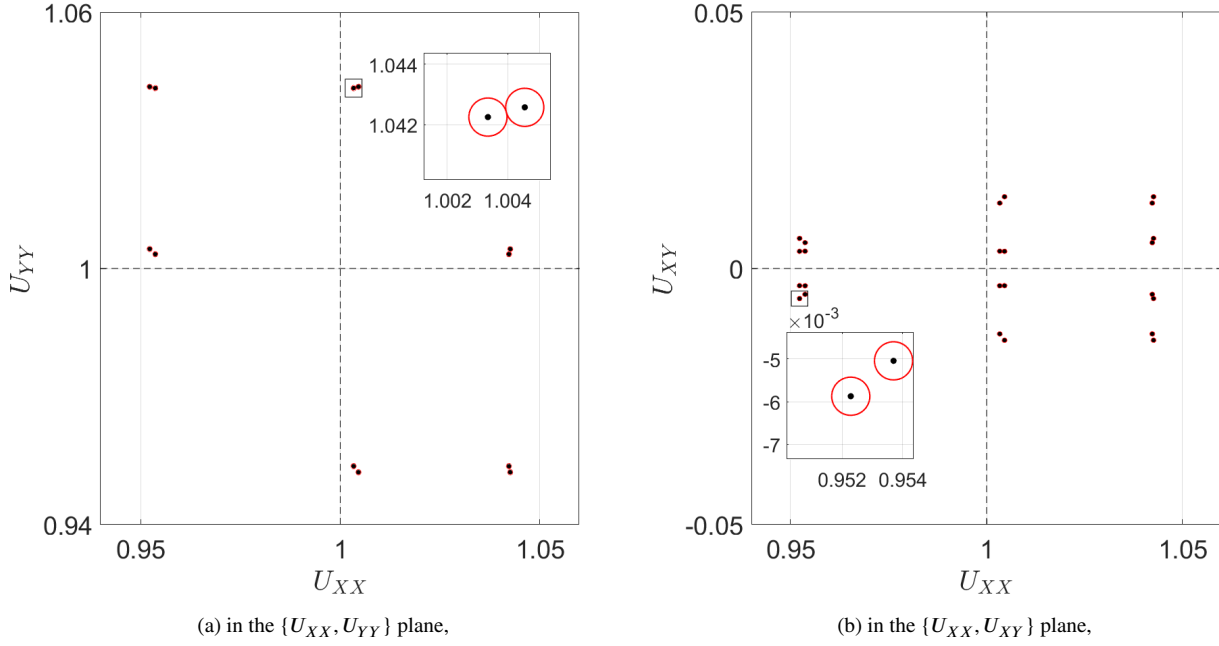


**Figure 5:** Mean right strain tensors  $\underline{U}_{ij}$  of different laminates (i,j) compatible with the austenite crystal, calculated from the stretch parameters given in Refs [38; 39]. Components refer here to the basis of the austenite cubic cell, namely  $\underline{X} = [100]$ ,  $\underline{Y} = [010]$ .

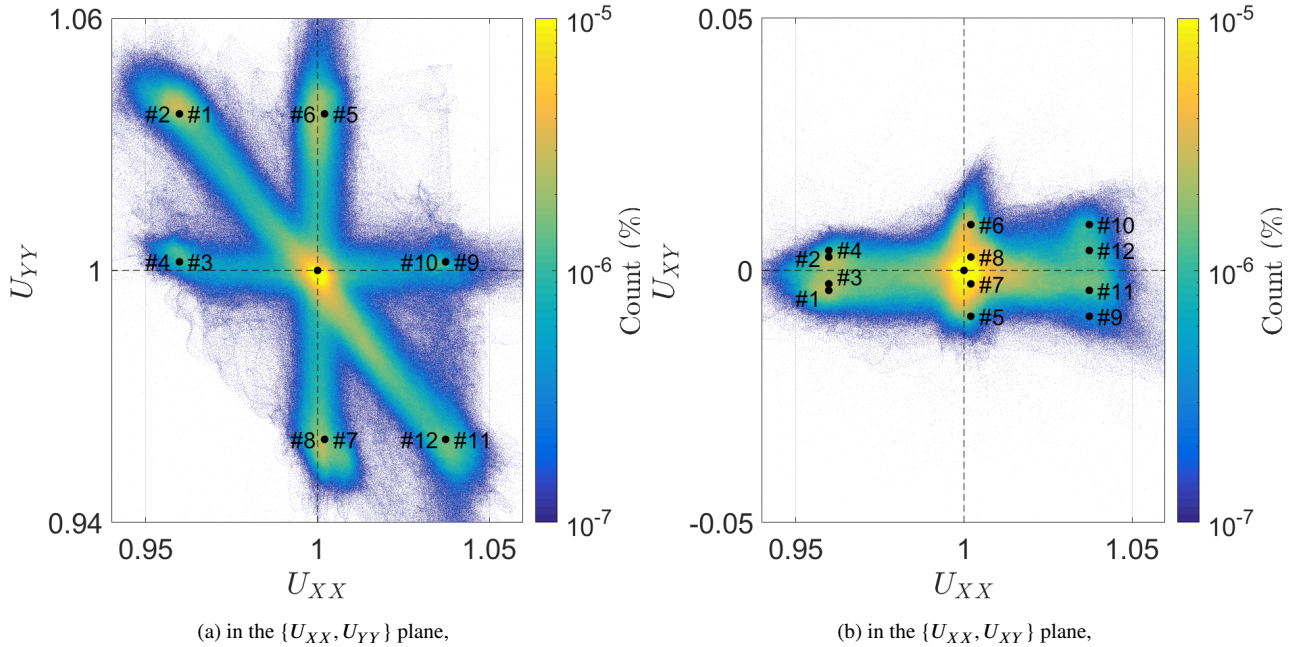


**Figure 6:** Experimental distribution of the in-plane components of the right strain tensor  $\underline{U}$  measured at the end of the first cooling stage (about  $-1^\circ\text{C}$ ). Components are expressed in the basis of the austenite crystal cell, namely  $\underline{X} = [100]$  and  $\underline{Y} = [010]$ . The numbers correspond to those of the identifiable habit plane variants (HPVs); see Table 2.

same number of distinct twins (two type-1 and two type-2), an equal proportion of all the variants or twins within the sample should correspond to the same intensity of martensite peaks in Fig. 7, which is not the case; see Section 4.6 for additional information about the self-accommodating character of the martensite created in the sample.

### 4.3. Analysis in the strain space

Comments can be made about the experimental strain distributions displayed above. See also Video 2 in the supplementary material showing variations in strain distribution during the first thermal cycle. It can be seen that the distributions are in very good agreement with the theory.

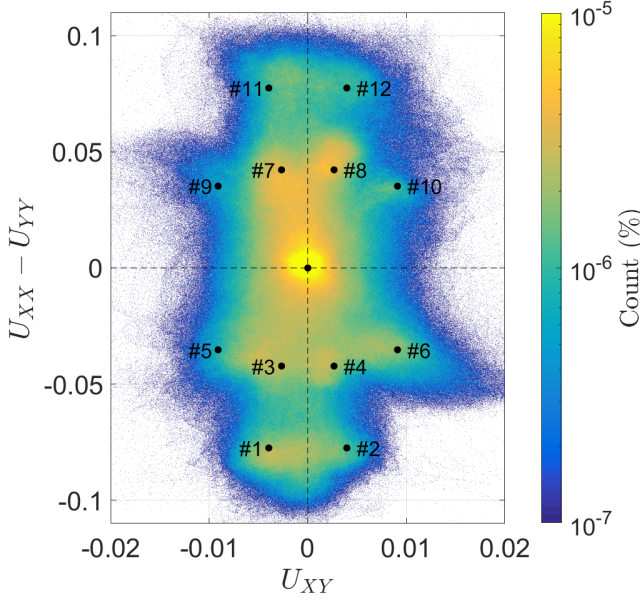


**Figure 7:** Same as Fig. 6 but in the  $\{U_{XY}, U_{XX} - U_{YY}\}$  plane.

**Table 2**

Martensite variants  $i$  and  $j$  potentially concerned in the experimentally identified martensite peaks, *i.e.* in the identifiable habit plane variants (HPVs). The variant numbers in the second column correspond to those in Eq. 5. The type of twin (type-1 or type-2) is labeled in superscript.

Martensite peak experimentally identified	Martensite twin $(i, j)$ potentially involved
HPV #1	$(4, 5)^I, (4, 5)^{II}, (4, 6)^I$ and $(4, 6)^{II}$
HPV #2	$(3, 5)^I, (3, 5)^{II}, (3, 6)^I$ and $(3, 6)^{II}$
HPV #3	$(1, 5)^{II}, (1, 6)^I, (2, 5)^I$ and $(2, 6)^{II}$
HPV #4	$(1, 5)^I, (1, 6)^{II}, (2, 5)^{II}$ and $(2, 6)^I$
HPV #5	Same as #1 but replacing $\lambda_{ij}$ by $1 - \lambda_{ij}$
HPV #6	Same as #2 but replacing $\lambda_{ij}$ by $1 - \lambda_{ij}$
HPV #7	Same as #3 but replacing $\lambda_{ij}$ by $1 - \lambda_{ij}$
HPV #8	Same as #4 but replacing $\lambda_{ij}$ by $1 - \lambda_{ij}$
HPV #9	$(1, 4)^I, (1, 4)^{II}, (2, 4)^I$ and $(2, 4)^{II}$
HPV #10	$(1, 3)^I, (1, 3)^{II}, (2, 3)^I$ and $(2, 3)^{II}$
HPV #11	Same as #9 but replacing $\lambda_{ij}$ by $1 - \lambda_{ij}$
HPV #12	Same as #10 but replacing $\lambda_{ij}$ by $1 - \lambda_{ij}$

For example, six peaks are found in the  $\{U_{XX}, U_{YY}\}$  plane (Fig. 6a). Their coordinates are similar to those of the theoretical predictions (black dots). In the other representation planes it may be more difficult to differentiate the different peaks, but the distributions reasonably match the theory. The highest peak (yellow in the images) corresponds to the presence of austenite, which here occupies almost 40% of the surface of the sample. The other peaks, corresponding to the various HPVs, consequently have much lower intensities. Note that the intensities of these peaks are different, which means that the HPV proportions are not equal within the

sample. This point will be discussed in detail in Section 4.6.

According to the theory in Section 3, the measured right strain tensor should only reach the states corresponding to the black dots. However, the experimental distributions appear to be diffuse around the dots. This can be explained by the presence of (small) elastic strains. The latter are *a priori* necessary to achieve kinematic compatibility at all the interfaces at the same time. However, strain states are also present far from the black dots: see for instance the “strain paths” between the black dots in Fig. 6a. This observation can be explained by the fact that the measurement method introduces smoothing (see Eq. 1) at the strain jumps. At the interfaces, strain values are thus smoothed over a distance corresponding here to 36 pixels (size of the Gaussian window  $g$  used). This explains the presence of strain paths between the austenite peak and the martensite peaks visible in Fig. 6a. However, surprisingly at first sight, it seems that there is no connection between the HPVs themselves. In fact, these connections do exist, as illustrated in Fig. 8. Three small rectangular areas containing an interface between two martensitic zones have been selected: see Fig. 8a. The distribution of the strain states over the red rectangle in Fig. 8b shows the connection between two martensite peaks, namely #2 and #12. It is worth noting that the latter have globally symmetric coordinates with respect to the center of the graph at  $(1, 1)$  representing the undeformed state. This allows this microstructure to minimize its overall strain. The same remark holds for the other two selected rectangular areas (white and black), implying other pairs of peaks that also tend to cancel each other out on average (see Figs 8c and 8d). As a general rule, martensite appears in the sample by involving pairs of HPVs so as to minimize their overall strain. Two additional comments can be made:

- The above general rule seems not to apply to the  $XY$  component: peaks #2 and #12 for the red rectangular area do not correspond to symmetrical  $U_{XY}$  values, as can be seen in Fig. 7 (both have  $U_{XY} > 0$ ). *Idem* with peaks #3 and #9 for the white rectangular area (here, both have  $U_{XY} < 0$ ). However, the  $XY$  strain values are much lower than those of the  $XX$  and  $YY$  strains (less than  $\pm 1\%$  vs. about  $\pm 4\%$ ), making the above general rule less critical for the  $U_{XY}$  component. We will see in the next section that the macroscopic  $XY$  strain remains low over the *whole* sample during the phase transition;
- The thin regular layering of strains visible on one side of the wedge in the black rectangular zone (Fig. 8a) makes its analysis complex: see Fig. 9 showing the associated distribution in the  $\{U_{XY}, U_{XX} - U_{YY}\}$  plane. In addition to the 12 theoretical dots corresponding to the identifiable HPVs, six red dots are displayed to represent the 6 individual martensite variants in Eq. 5. The strain layering probably corresponds to the twinning of two variants  $\underline{U}_i$  and  $\underline{U}_j$ . However, the spatial resolution does not enable a clear identification

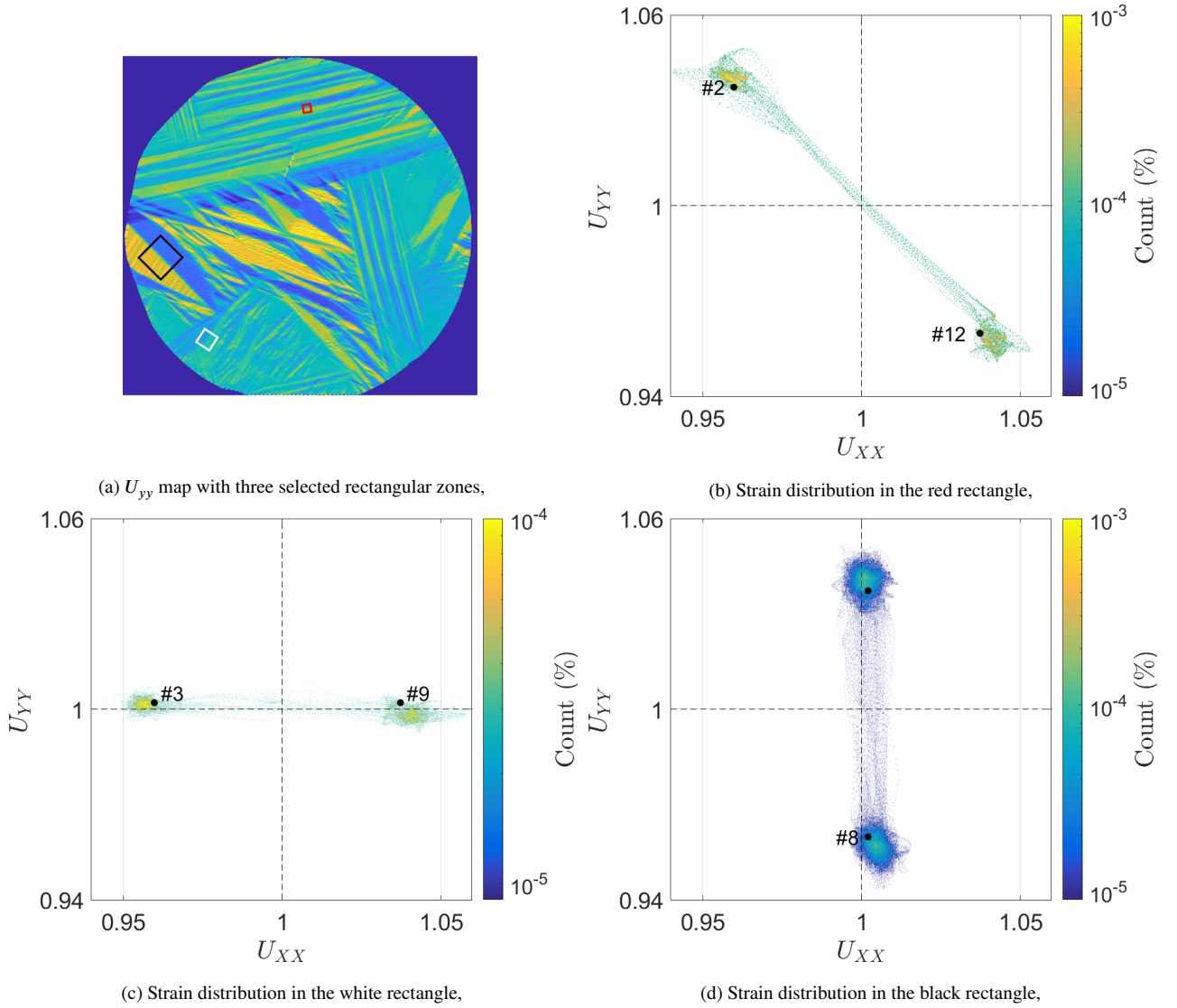


**Figure 8:** Evidencing the connections between martensite peaks at interfaces between two martensitic zones (here at 267.45 s,  $-0.76^\circ\text{C}$ ).

due to the strong strain smoothing caused by LSA in this zone composed of close strain jumps. The deconvolution of the images to identify smaller details in the strain maps is a future prospect of this work; see Section 5.

#### 4.4. Variations in macroscopic strain

Figure 10a shows variations in the in-plane components of the macroscopic strain  $\langle \underline{E} \rangle$  defined by  $\langle \underline{E} \rangle = \langle \underline{U} \rangle - \underline{I}$ , calculated over the whole sample surface during the cooling stage. The temperature variation is also indicated in the graph. It can be seen that the three strain components first increase in magnitude. This can be explained by the increasing proportion of HPV pairs that do not create perfectly zero strains on average. Thereafter, the values fluctuate sharply, and globally decrease before stabilization. In particular, several rapid drops in strain magnitude are visible. These correspond to the rapid appearance of new martensite

microstructures, selected *a priori* because they reduce the level of elastic energy in the sample. The mean change in slope of the temperature curve from about 130 s ( $\approx 3^\circ\text{C}$ ) can be attributed to a strong release of latent heat after a slow transformation initiation. Finally, we note that the overall level of macroscopic strain remained very low during the phase transformation (compared to strain levels of several percent in the individual HPVs). The following values were measured at the end of cooling:  $\langle \underline{E} \rangle_{xx} \approx -0.01\%$ ,  $\langle \underline{E} \rangle_{yy} \approx -0.07\%$  and  $\langle \underline{E} \rangle_{xy} \approx +0.02\%$ . This shows the strong self-accommodating character, at the macroscopic scale, of the phase transformation. It will be seen below that self-accommodation is not the result of equal HPV proportions within the sample.

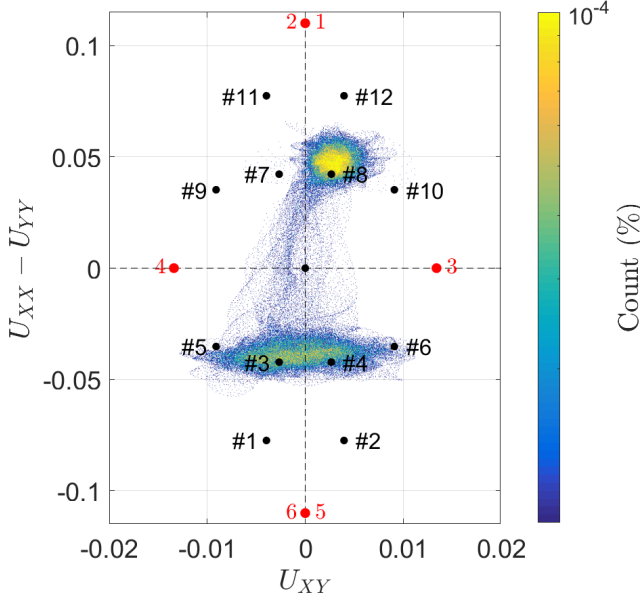


**Figure 9:** Experimental strain distribution in the  $\{U_{XY}, U_{XX} - U_{YY}\}$  plane over the black rectangular area in Fig. 8a (inside a wedge). The six red dots correspond to the 6 martensite variants in Eq. 5. The layering of strains on one side of the wedge does not allow a clear identification of the variants involved, due to the strong strain smoothing caused by LSA in this zone.

#### 4.5. Does austenite deform during the phase transformation?

Elementary stress-free microstructures with few interfaces are theoretically subject to specific restrictions on the stretch parameters [2; 4]. However, in the case of complex microstructures involving a large number of interfaces, global compatibility is likely to require additional elastic strains whatever the stretch parameter values. The question of the internal stress level is critical, as stresses influence the kinetics of phase transformation. This question is addressed here by considering the strain field in the austenite zones. Small fluctuations in  $\underline{U}$  around the identity matrix are an indicator of stresses in austenite. Figure 11 shows two  $U_{yy}$  maps during the cooling stage of the sample: at 10.83 °C (at 89.36 s) and at 5.04 °C (at 118.01 s). The color scale has been set to a small range around 1, namely [0.997; 1.003], to highlight the small (elastic) strains. Heterogeneous strain fields are clearly visible in austenite: see the color gradient from light blue to light green. Values below and above 1 are present, evidencing compression and tension states respectively. It can be observed that the compression states (light blue) are mainly in the middle of the sample. The same applies to the  $U_{xx}$  distributions (maps not presented here). This stressed state may explain the appearance of the central microstructure (in yellow in the maps) which is not connected to the sample boundary. It can be also noted that the compression level in the austenite in the middle of the sample increases when the quantity of martensite increased:

the blue color becomes darker from Fig. 11a to Fig. 11b. Figure 10b shows the variation in macroscopic strain in the austenite only, as well as the temperature variation. There is an initial increase in strain magnitude as it was visualized with Figs 11a and 11b, followed by rapid fluctuations tending to limit the average strain level:  $\langle \underline{E} \rangle_{xx} \approx -0.01\%$ ,  $\langle \underline{E} \rangle_{yy} \approx -0.08\%$  and  $\langle \underline{E} \rangle_{xy} \approx +0.03\%$  in the austenite at the end of the cooling. The thresholding/decreasing of the macroscopic strain from around 130 s ( $\approx 3$  °C) is associated with a lower slope of the temperature curve, showing that the calorific character of the phase transformation (latent heat release) accompanies its kinematic evolution.

#### 4.6. Are the HPVs equally represented within the sample?

It is often considered in macroscopic models that the martensite variants are equally created during a temperature-induced transformation without external mechanical loading. This assumption is acceptable in the case of polycrystals with numerous small-scale microstructures. The situation is *a priori* different in the case of a single-crystal sample. Indeed, the spatio-temporal evolution of the phase transformation at a given time is expected to be influenced by the kinematic and energetic state of the sample resulting from the microstructures that are already created. Typically, the appearance of a specific HPV at a given time influences the rest of the phase transformation of the sample, and an equal proportion of HPVs over the sample is unlikely.

In this context, the present section aims to study the variations in HPV proportions during the cooling of the sample. The calculation of the proportions was performed as follows. First, the  $\underline{U}$  tensor measured at each pixel was associated with its closest theoretical counterpart (numbered from #1 to #12; see Table 2) with respect to the Euclidean norm in the  $\{U_{xx}, U_{yy}, U_{xy}\}$  space. Second, we considered only experimental  $\underline{U}$  tensors in the “neighborhood” of the theoretical ones, namely at a distance lower than or equal to 0.012 from the theoretical counterpart. This enabled us to ignore data altered by smoothing at the interfaces. Finally, the percentages of the 12 martensite twins were calculated at each time during the cooling stage. Figures 12a to 12c show the histograms at the same three times as in Fig. 4. The total percentages of martensite are also indicated at the top of the graphs. The spatial distribution at the same times is shown in Figs 12d to 12f. Austenite is indicated by “A” in the color bars. Note that the white zones in the maps correspond to the pixels for which the experimental  $\underline{U}$  tensors are not in the neighborhood of a theoretical one. It can be seen that these white zones correspond to interfaces, justifying their removal from the analysis because of the smoothing effect. The following comments can be made from these figures:

- When the sample reached 5 °C during cooling (Figs 12a and 12d), the proportion of martensite estimated from the maps was about 5%. The HPV proportions appear to be different from each other. Indeed, some HPVs

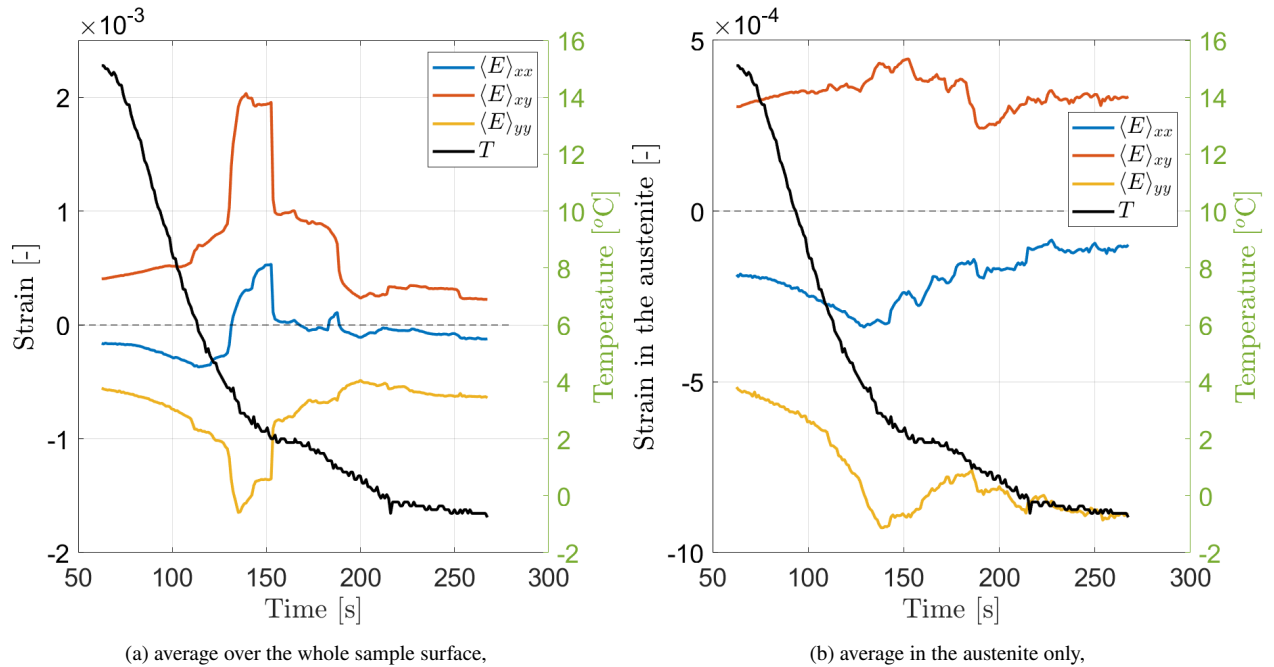


**Figure 10:** Variation in macroscopic strain components and temperature during the cooling stage of the first thermal cycle. The low strain levels show the self-accommodating character, at the macroscopic scale, of the martensite created.

are preferentially formed (#5, #6 and #8) while others have not yet appeared (#2 and #11);

- At the end of the cooling stage (about  $-1^\circ\text{C}$ , Figs 12b and 12e), more than half the sample is transformed, and all 12 identifiable HPVs are present. Here too, there are marked differences in the proportions of the HPVs. It may be noted that the percentages are not ranked in the same way as those obtained at  $5^\circ\text{C}$ . The difference between the lowest (about 1.9% for HPVs #4, #9 and #10) and highest (8.3% for HPV #1) is significant, and it can be noted that the highest value already corresponds to 1/12 (the ratio obtained if all HPVs had the same probability of occurrence);
- At end of heating (about  $45^\circ\text{C}$ , Figs 12c and 12f), before the beginning of the second thermal cycle, residual martensitic microstructures are visible. However, despite their negligible quantity (0.4%), they may alter the phase transformation kinetics of the following thermal cycle. The question of repeatability over the three thermal cycles is discussed in the next section.

#### 4.7. Is the observed microstructure repeatable?

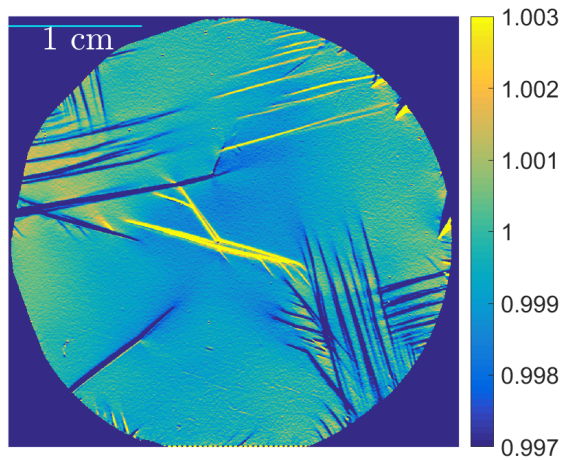
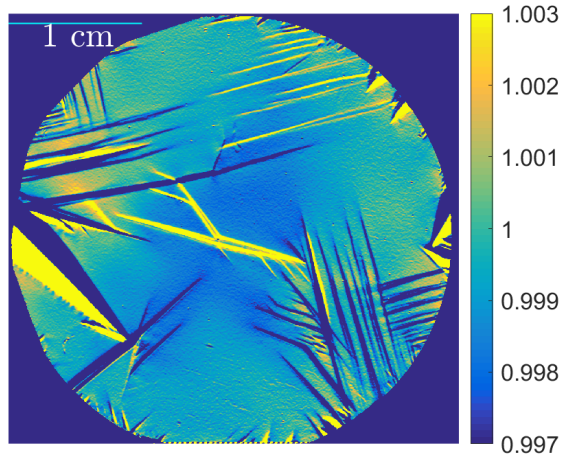
The question of the repeatability of the spatio-temporal kinetics of transformation can now be discussed. It is worth recalling that the sample was previously trained by numerous transformation cycles. However, the presence of residual martensite at the end of any thermal cycle potentially impacts the repeatability of the transformation. To assess the level of repeatability, the proportions of HPVs as well as

their spatial distributions at the end of the three cooling stages are shown in Fig. 13. See also Video 3 in the supplementary material. Several observations can be made:

- From the three spatial distributions (Figs 13d, 13e and 13f), it can be observed that the microstructures, despite not being strictly identical, are very similar. There are slight local differences, but similar general patterns are observed. The main difference lies in the non-recurrence of the centimetric wedge observed in the lower left-hand part of the sample during the first cycle;
- At the macroscopic scale, the histograms in Figs 13a, 13b and 13c support the fact that the sample globally forms its HPVs in a repeatable manner. In particular, HPVs #1 and #7 are always preferentially created during the different cycles. However, there is a noticeable increase in the overall proportion of martensite over the cycles: 57.5%, then 59.7% and finally 61.2%. The study of repeatability over many cycles starting from a virgin sample is a future prospect of this work, as indicated in the conclusion section.

## 5. Conclusion

In this study, Localized Spectrum Analysis (LSA) was employed to track the strain components associated with habit plane variants (HPVs) in a  $\text{Cu-Al}_{13.9}\text{-Ni}_{4.6}$  (wt.%) single crystal subjected to thermal cycles. Using a specific surface preparation (depositing a checkerboard pattern on the surface of the sample) and an optical device involving

(a)  $U_{yy}$  at 89.36 s, 10.83 °C(b)  $U_{yy}$  at 118.01 s, 5.04 °C

**Figure 11:** Evidencing small (elastic) strains in the austenite:  $U_{yy}$  fields at two times during the cooling of the sample. Note that the values have been thresholded to better visualize the gradients in austenite.

a 28 Mpixel camera, a relevant trade-off between strain resolution ( $2 \times 10^{-4}$ ) and spatial resolution (0.26 mm) over the sample's 33 mm diameter circular surface was obtained. This enabled us to measure the components of the *mean* right strain tensor  $\underline{U}$  associated with the different identifiable HPVs. The following results were obtained:

- A good agreement was observed between experimental data and theoretical expectations relying on the compatibility between orthorhombic martensite laminates and austenite. It was possible to identify the stretch parameters associated with the cubic-to-orthorhombic transformation from the strain measurements.
- It was also observed that the process of martensite formation during cooling is based on the coordinated activation of HPVs pairs whose strain levels globally compensate each other.

- Small (elastic) strains were also experimentally evidenced in austenite, highlighting the need for additional deformation to achieve kinematic compatibility at the microstructure interfaces.
- Using a sample trained by numerous transformation cycles, the level of phase transformation repeatability appeared to be high, with only small differences in the obtained microstructures. In addition, the spatio-temporal kinetics of martensite appearance and disappearance appeared to be roughly symmetrical: the microstructures that appeared first are generally those that disappeared last.

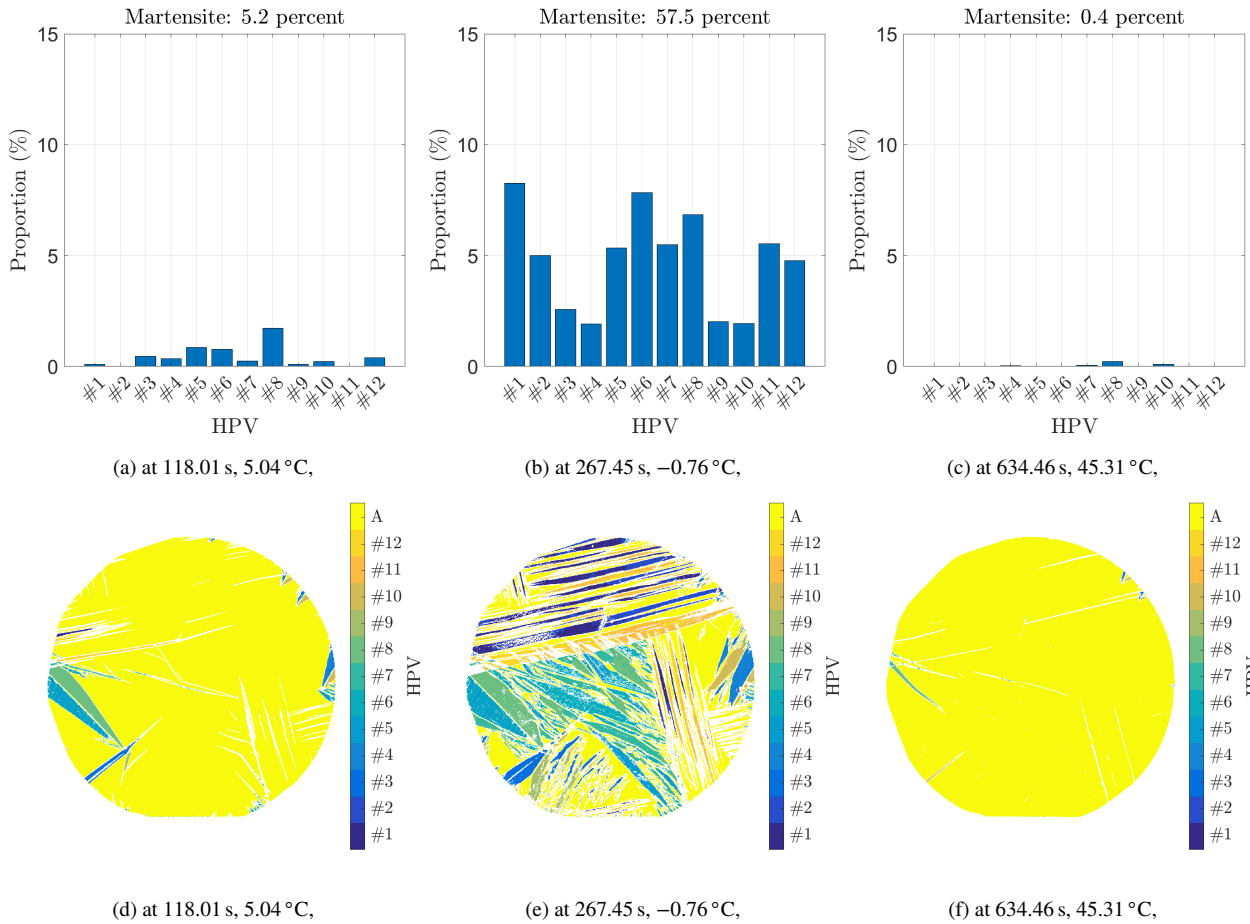


**Figure 12:** Proportion and spatial distribution of the habit plane variants (HPVs) during the first thermal cycle. First column: at about 5 °C during cooling. Second column: at the end of cooling (about -1 °C). Third column: at end of heating (about 45 °C). See also Video 3 in supplementary material.



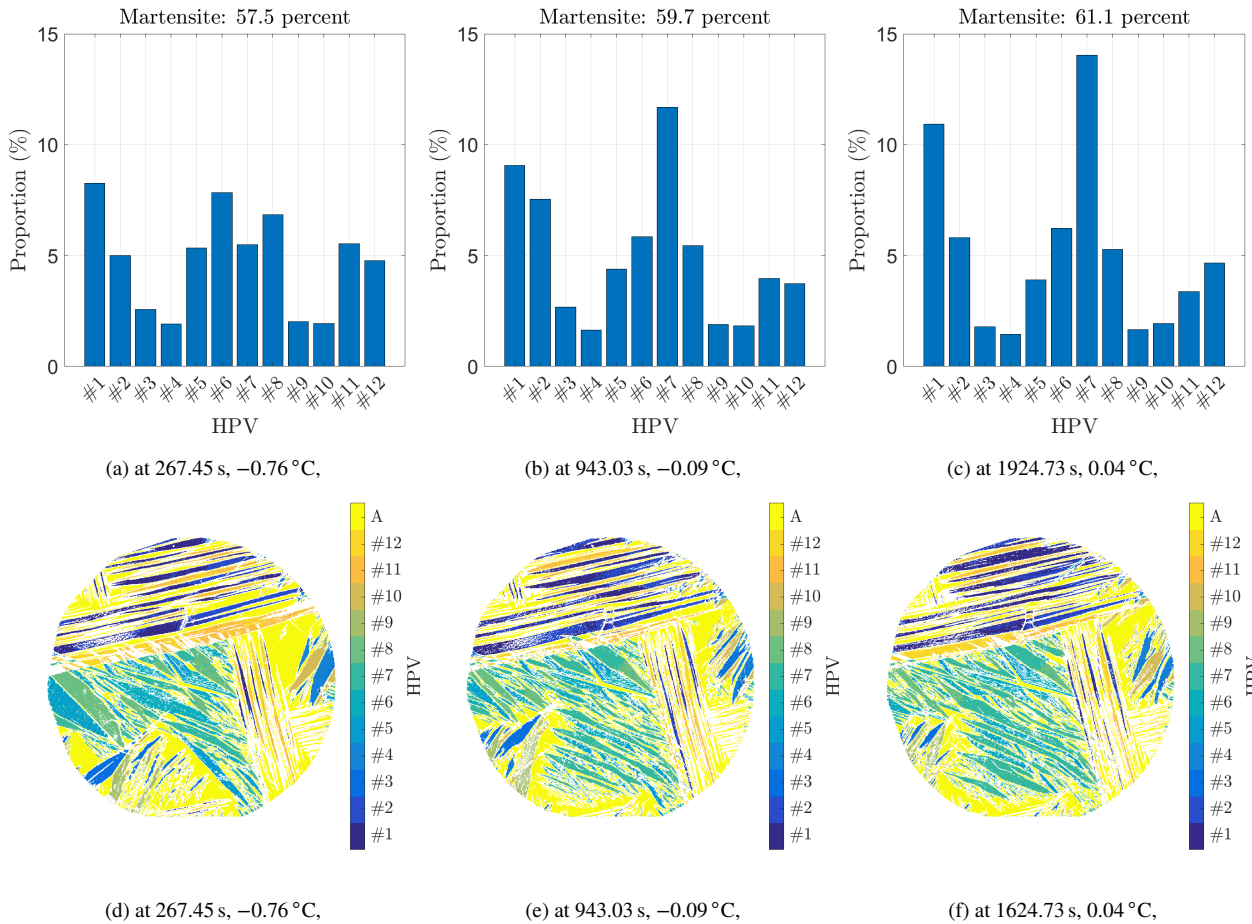


**Figure 13:** Repeatability of the phase transformation: proportion and spatial distribution of the HPV types at the end of each cooling stage of the experiment. First column: end of first cycle. Second column: end of second cycle. Third column: end of third cycle. See also Video 3 in supplementary material.

## Declaration of Competing interests

The authors declare that they have no competing interests.

## Data availability

Data will be made available on request.

## Acknowledgement

The authors acknowledge the I-SITE CAP20-25 program for its financial support during this research through the Emergence 2022 project. This work was also sponsored by the AURA regional council and the French government research program “Investissements d’Avenir” through the IDEX-ISITE initiative 16-IDEX-0001 (CAP 20-25). The authors acknowledge support from the ANR Grant ANR-18-CE08-0028-01. They also thank Professors E. Vives and G. Zanzotto for fruitful discussions.

## References

- [1] K. Otsuka, C. Wayman, Shape memory materials, Cambridge: Cambridge University Press, 1999.
- [2] R. D. James, K. F. Hane, Martensitic transformations and shape-memory materials, *Acta Materialia* 48 (2000) 197–222.
- [3] M. Pitteri, G. Zanzotto, Continuum models for phase transitions and twinning in crystals, Chapman and Hall/CRC, 2002.
- [4] K. Bhattacharya, Microstructure of martensite: why it forms and how it gives rise to the shape-memory effect, Vol. 2, Oxford University Press, 2003.
- [5] M. Wechsler, D. Lieberman, T. Read, On the theory of the formation of martensite, *Transactions of the Metallurgical Society of AIME* 197 (1953) 1503–1515.
- [6] J. Bowles, The crystallography of martensitic transformation I and II, *Acta Metallurgica* 2 (1954) 129–147.
- [7] A. Roitburd, Martensitic transformation as a typical phase transformation in solids, *Solid State Physics* 33 (1978) 317–390.
- [8] J. Ericksen, Some phase transitions in crystals, *Archive for Rational Mechanics and Analysis* 73 (1980) 99–124.
- [9] G. Barsch, J. Krumhansl, Twin boundaries in ferroelastic media without interface dislocations, *Physical Review Letters* 53 (1984) 1069.
- [10] J. M. Ball, R. D. James, Fine phase mixtures as minimizers of energy, *Archive for Rational Mechanics and Analysis* 100 (1987) 267–318.
- [11] S. Stupkiewicz, G. Maciejewski, H. Petryk, Low-energy morphology of the interface layer between austenite and twinned martensite, *Acta Materialia* 55 (2007) 6292–6306.
- [12] X. Balandraud, G. Zanzotto, Stressed microstructures in thermally induced M9R-M18R martensites, *Journal of the Mechanics and Physics of Solids* 55 (2007) 194–224.
- [13] H. Seiner, O. Glatz, M. Landa, Interfacial microstructures in martensitic transitions: from optical observations to mathematical modeling, *International Journal for Multiscale Computational Engineering* 7 (2009) 445–456.
- [14] X. Balandraud, D. Delpueyo, M. Grédiac, G. Zanzotto, Almost compatible microstructures in shape memory alloys, *Acta Materialia* 58 (14) (2010) 4559–4577.
- [15] H. Petryk, S. Stupkiewicz, Interfacial energy and dissipation in martensitic phase transformations. Part I: Theory, *Journal of the Mechanics and Physics of Solids* 58 (2010) 390–408.
- [16] S. Stupkiewicz, G. Maciejewski, H. Petryk, Elastic micro-strain energy of austenite–martensite interface in NiTi, *Modelling and Simulation in Materials Science and Engineering* 20 (2012) 035001.
- [17] S. Stupkiewicz, A. Gorzyska-Lengiewicz, Almost compatible X-microstructures in CuAlNi shape memory alloy, *Continuum Mechanics and Thermodynamics* 24 (2012) 149–164.
- [18] H. Seiner, Mobile interfacial microstructures in single crystals of Cu–Al–Ni shape memory alloy, *Shape Memory and Superelasticity* 1 (2015) 268–274.
- [19] E. Bronstein, E. Faran, D. Shilo, Analysis of austenite-martensite phase boundary and twinned microstructure in shape memory alloys: The role of twinning disconnections, *Acta Materialia* 164 (2019) 520–529.
- [20] H. Seiner, P. Plucinsky, V. Dabade, B. Benesova, R. James, Branching of twins in shape memory alloys revisited, *Journal of the Mechanics and Physics of Solids* 141 (2020) 103961.
- [21] D. Shilo, E. Faran, B. Karki, P. Mullner, Twin boundary structure and mobility, *Acta Materialia* 220 (2021) 117316.
- [22] S. Stupkiewicz, M. Rezaee-Hajidehi, H. Petryk, Multiscale analysis of the effect of interfacial energy on non-monotonic stress–strain response in shape memory alloys, *International Journal of Solids and Structures* 221 (2021) 77–91.
- [23] Y. He, Interface propagation and energy dissipation in shape memory alloys, *Scripta Materialia* 230 (2023) 115420.
- [24] G. Qin, C. Zhang, S. Zhang, X. Chen, Y. He, Compatibility effect on stress-free two-way memory of Ni-Mn-Ga single crystal, *Journal of Alloys and Compounds* 935 (2023) 168134.
- [25] H. Fidder, I. Basu, J. T. DeHosson, Twinning induced spatial stress gradients: Local versus global stress states in hexagonal close-packed materials, *Acta Materialia* 256 (2023) 119142.

- [26] C. Zhang, X. Balandraud, Y. He, Coexistence of five domains at single propagating interface in single-crystal Ni-Mn-Ga shape memory alloy, *Journal of the Mechanics and Physics of Solids* 183 (2024) 105481.
- [27] D. Delpueyo, A. Jury, X. Balandraud, M. Grediac, Applying full-field measurement techniques for the thermomechanical characterization of shape memory alloys: a review and classification, *Shape Memory and Superelasticity* 7 (2021) 462–490.
- [28] G. Bomarito, J. Hochhalter, T. Ruggles, A. Cannon, Increasing accuracy and precision of digital image correlation through pattern optimization, *Optics and Lasers in Engineering* 91 (2017) 73–85.
- [29] S. Fayad, D. Seidl, P. Reu, Spatial dic errors due to pattern-induced bias and grey level discretization, *Experimental Mechanics* 60 (2020) 249–263.
- [30] F. Sur, B. Blaysat, M. Grediac, On biases in displacement estimation for image registration, with a focus on photomechanics, *Journal of Mathematical Imaging Vision* 63 (2021) 777–806.
- [31] D. Delpueyo, M. Grediac, X. Balandraud, C. Badulescu, Investigation of martensitic microstructures in a monocrystalline Cu–Al–Be shape memory alloy with the grid method and infrared thermography, *Mechanics of Materials* 45 (2012) 34–51.
- [32] X. Balandraud, N. Barrera, P. Biscari, M. Grediac, G. Zanzotto, Strain intermittency in shape-memory alloys, *Physical Review B* 91 (2015) 174111.
- [33] B. Blaysat, X. Balandraud, M. Grediac, E. Vives, N. Barrera, G. Zanzotto, Concurrent tracking of strain and noise bursts at ferroelastic phase fronts, *Communications Materials* 1 (2020) 3.
- [34] F. Sur, B. Blaysat, M. Grediac, On biases in displacement estimation for image registration, with a focus on photomechanics, *Journal of Mathematical Imaging and Vision* 63 (2021) 777–806.
- [35] T. Massalski, U. Mizutani, Electronic-structure of hume-rothery phases, *Progress in Materials Science* 22 (1978) 151–262.
- [36] L. Carrillo, L. Mañosa, J. Ortín, A. Planes, E. Vives, Experimental evidence for universality of acoustic emission avalanche distributions during structural transitions, *Physical Review Letters* 81 (1998) 1889–1892.
- [37] V. Recarte, R. Perez-Saez, J. San Juan, E. Bocanegra, M. No, Influence of al and ni concentration on the martensitic transformation in Cu-Al-Ni shape-memory alloys, *Metallurgical and Materials Transactions A* 33 (2002) 2581–2591.
- [38] K. Otsuka, K. Shimizu, Morphology and crystallography of thermoelastic  $\gamma'$  cu-al-ni martensite, *Japanese Journal of Applied Physics* 8 (10) (1969) 1196.
- [39] K. Bhattacharya, Wedge-like microstructure in martensites, *Acta Metallurgica et Materialia* 39 (10) (1991) 2431–2444.
- [40] Y. Surrel, Printing grids at the University of Southampton print centre., Internal report, University of Southampton (2017).
- [41] Y. Surrel, Printing grids at the University of Southampton Print Centre - Using the "high quality" mode., Internal report, University of Southampton (2017).
- [42] L. Fletcher, J. V. Blitterswyk, F. Pierron, A manual for conducting image-based inertial impact (ibii) tests, Project Report 10.5258/SO-TON/P0015 (August 2019).
- [43] R. Moulart, R. Rotinat, F. Pierron, G. Lerondel, On the realization of microscopic grids for local strain measurement by direct interferometric photolithography, *Optics and Lasers in Engineering* 45 (12) (2007) 1131–1147.
- [44] R. Moulart, R. Rotinat, F. Pierron, Full-field evaluation of the onset of microplasticity in a steel specimen, *Mechanics of Materials* 41 (11) (2009) 1207–1222.
- [45] J.-L. Piro, M. Grédiac, Producing and transferring low-spatial-frequency grids for measuring displacement fields with moire and grid methods, *Experimental Techniques* 28 (4) (2004) 23–26.
- [46] Q. Bouyra, B. Blaysat, H. Chanal, M. Grédiac, Using laser marking to engrave optimal patterns for in-plane displacement and strain measurement, *Strain* 58 (2) (2022).
- [47] F. Sur, B. Blaysat, M. Grédiac, Determining displacement and strain maps immune from aliasing effect with the grid method, *Optics and Lasers in Engineering* 86 (2016) 317–328.
- [48] J. Réthoré, A fully integrated noise robust strategy for the identification of constitutive laws from digital images, *International Journal for Numerical Methods in Engineering* 84 (6) (2010) 631–660.
- [49] M. Grédiac, B. Blaysat, F. Sur, Extracting displacement and strain fields from checkerboard images with the localized spectrum analysis, *Experimental Mechanics* 59 (2) (2019) 207–218.
- [50] M. Grédiac, F. Sur, B. Blaysat, The grid method for in-plane displacement and strain measurement: A review and analysis: The grid method, *Strain* 52 (3) (2016) 205–243.
- [51] M. Grédiac, B. Blaysat, F. Sur, Comparing several spectral methods used to extract displacement fields from checkerboard images, *Optics and Lasers in Engineering* 127 (2020) 105984.
- [52] F. Sur, M. Grédiac, Towards deconvolution to enhance the grid method for in-plane strain measurement, *Inverse Problems and Imaging* 8 (1) (2014) 259–291, American Institute of Mathematical Sciences.
- [53] E. Grafarend, Linear and nonlinear models: fixed effects, random effects, and mixed models, De Gruyter, 2006, Walter de Gruyter. ISBN-13:978-3-11-016216-5.